Localized mix-induced radiative cooling in a capsule implosion at the National Ignition Facility

B. Bachmann,[1,*] J. E. Ralph,[1] A. B. Zylstra,[1,2] S. A. MacLaren,[1] T. Döppner,[1] D. O. Gericke,[3] G. W. Collins,[4,5] O. A. Hurricane,[1] T. Ma,[1] J. R. Rygg,[4,5] H. A. Scott,[1] S. A. Yi,[2] and P. K. Patel[1]

[1]*Lawrence Livermore National Laboratory, Livermore, California 94551, USA*

[2]*Los Alamos National Laboratory, Los Alamos, New Mexico 87545, USA*

[3]*Centre for Fusion, Space and Astrophysics, Department of Physics, University of Warwick, Coventry CV4 7AL, United Kingdom*

[4]*Departments of Mechanical Engineering, Physics and Astronomy, University of Rochester, Rochester, New York 14623, USA*

[5]*Laboratory for Laser Energetics, University of Rochester, Rochester, New York 14623, USA*

(Received 19 July 2019; accepted 25 February 2020; published 17 March 2020)

We present direct measurements of electron temperature variations within an inertially confined deuterium-tritium plasma caused by localized mix of higher-Z materials into the central hot spot. The data are derived from newly developed differentially filtered penumbral imaging of the bremsstrahlung continuum emission. Our analysis reveals distinct localized emitting features in the stagnated hot-spot plasma, and we infer spatial variations in the electron temperature: the mixed region is 660 ± 130 eV colder than the surrounding hot-spot plasma at 3.26 ± 0.11 keV. Our analysis of the energy flow shows that we measure approximately steady-state conditions where the radiative losses in the mix region are balanced by heat conduction from the surrounding hot deuterium-tritium plasma.

DOI: 10.1103/PhysRevE.101.033205

I. INTRODUCTION

Spherical implosions are a highly efficient method to create extreme densities and temperature conditions in the laboratory. One major application are experiments on inertial confinement fusion (ICF) as pursued at the National Ignition Facility (NIF) [1–4]. The indirect drive configuration [5] at NIF uses a hohlraum to convert the laser energy of NIF's 192 beams into x-rays that rapidly ablate the surface of a thin, millimeter-radius shell. The ablation pressure causes a radially inward acceleration designed to reach velocities above 350 km/s and kinetic energies >20 kJ, which compresses and heats the 50/50 deuterium-tritium (D-T) vapor at the capsule core to a pressure of >250 Gbar and ion temperature of >4 keV. In this hot spot, the D-T reactivity is high enough to initiate enough fusion events that further heat the plasma by the energetic α particles created. Understanding how kinetic energy of spherically imploding shells transforms into compression and heat and ultimately results in thermonuclear burn is a major challenge on the path towards ignition. In particular, the effective mitigation of the various instabilities still poses an eminent challenge.

The injection of any other material into the central hot D-T plasma core leads to increased energy losses as electrons that interact with higher charges will produce continuum radiation more efficiently. Ablator material can be injected into the hot spot when instabilities, such as Rayleigh-Taylor and Richtmyer-Meshkov, grow from surface defects, capsule debris, inhomogeneities in the bulk of crystalline ablators, or engineering features such as the fill-tube [6–10]. The resulting radiation losses remain a key loss mechanism in current implosions, especially at the highest performance level [11–13]. Understanding and mitigating hot-spot mixing is thus essential on the pathway toward ignition and high gain burn.

In prior studies [14–17], it was unclear whether the observed bright, localized features in x-ray self-emission images were caused by the mix of a small amount of ablator material in the hot D-T plasma or if the mix region contains significantly more high-Z material emitting at a lower temperature. Both scenarios are plausible and while requiring different mitigation strategies, they cannot be distinguished by their total or relative measured brightness. It is thus key to quantify the local temperature of the bright features within the hot spot.

Here we demonstrate experimentally that radiation losses can significantly lower the temperature of a confined region in the hot spot. While also applicable to other sources of mix, we focus on a case where mix is caused by the fill-tube perturbation that produces an inward-directed jet transporting ablator material into the central hot spot. Similar radiation has been observed in many fusion experiments [14–21] and is hypothesized to be a primary source of neutron yield degradation for the best performing implosions on the NIF to date [13].

Our measurements of temperature variations are based on penumbral images of the central hot spot using its hard x-ray (19 and 22 keV) emission and have high signal-to-noise (500–1000), high-spatial resolution (5 μm), and high dynamic range (16 bit). They allow one to detect spatial variations of the electron temperature caused by the radiation losses during peak compression of the D-T plasma. Our measurements show that, averaged over the burn duration and the localized region with mix, the temperature is reduced by 660 ± 130 eV from the surrounding 3.26 ± 0.11 keV hot-spot plasma. In the center of the mix, we find even larger reductions. Moreover,

*bachmann2@llnl.gov

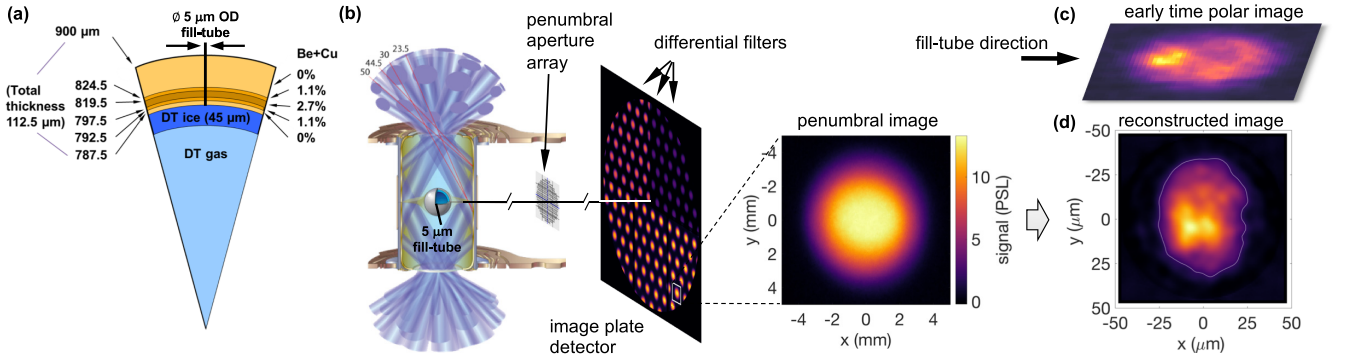

FIG. 1. (a) Cross section of the beryllium capsule with Cu dopant fractions [25]. (b) Diagram of the indirect drive hohlraum configuration, showing the x-ray penumbral imaging configuration and raw data for implosion N180121-2, imaged through an array of approximately 100 penumbral apertures with 100 μm diameter each and filtered with a series of x-ray differential filters. (c) Early-time, soft x-ray image captured from the north pole of the target chamber, approximately 50 ps before peak x-ray emission, tracking the bright feature coming from the direction of the fill tube. (d) Reconstructed penumbral image of the equatorial hot-spot emission (axis 90–100), orthogonal to the fill-tube axis. Increased x-ray emission from the fill-tube jet is clearly visible in the center.

we find that heat conduction into the mix and radiative losses balance each other during the x-ray emission.

II. EXPERIMENTAL PROCEDURE

The set-up of our experiment is shown in Fig. 1. For this study, we use a beryllium ablator shell with graded copper-doping that has a 45 μm-thick D-T ice fuel layer on the inside [see Fig. 1(a)]. The D-T fuel is filled into the capsule through a fill-tube with 5 μm diameter. The implosion (N180121-2) is driven by 1.2 MJ laser energy with 320 TW peak power [21–25]. The drive is designed such that only 5% to 10% of the ablator is remaining at the time of peak compression. At this time, conditions are sufficient for α particle production in the hot spot. Whereas the associated neutrons are used as additional diagnostics, the fusion rate on these subscale experiments is too low to initiate a burn wave and ignition of the entire D-T fuel.

In order to measure hot-spot temperature variation with sufficient spatial resolution and signal-to-noise, an array of circular apertures orthogonal to the fill-tube axis collects a series of x-ray penumbral images of the plasma inside the capsule [see Fig. 1(b)] [26]. These images are filtered with a variety of hard x-ray filters [see Figs. 2(a)–2(c)], detected with high signal-to-noise (500–1000) via an image plate, and reconstructed using computed tomography techniques to produce x-ray images of the imploding hot spot with a spatial resolution of 5 μm [27]. For this shot, we used a 103.5 ± 0.5 μm and a 207 ± 1 μm-thick titanium filter in addition to a 2.7 mm polycarbonate debris shield and 460 μm of Kapton, which is common to all x-ray channels in this setup. Through these filters, we measure the x-ray distribution at emission weighted average x-ray energies of 19 and 22 keV, respectively.

The resolution is adequate for resolving the localized bright region shown in Fig. 1(d). Compared to typically fielded 10 μm diameter pinholes with ≈ 12 μm spatial resolution, the larger penumbral apertures increase the photon flux by a factor of approximately 36. This allows measurements with high signal-to-noise at higher x-ray energies that are less affected by ablator absorption. This combination enables the measurements of local temperatures presented here.

The reason for the clearly visible region with enhanced x-ray emission in Fig. 1(d) is a significant mix of D-T plasma with ablator material, initiated by the fill-tube perturbation. This can be seen from a time-resolved framing camera pinhole image taken from the target chamber pole and earlier in time, which shows the jet moving inwards along the fill-tube axis [Fig. 1(c)].

III. DATA ANALYSIS

The local temperature of the mix region is obtained using a Fourier mode decomposition of the reconstructed

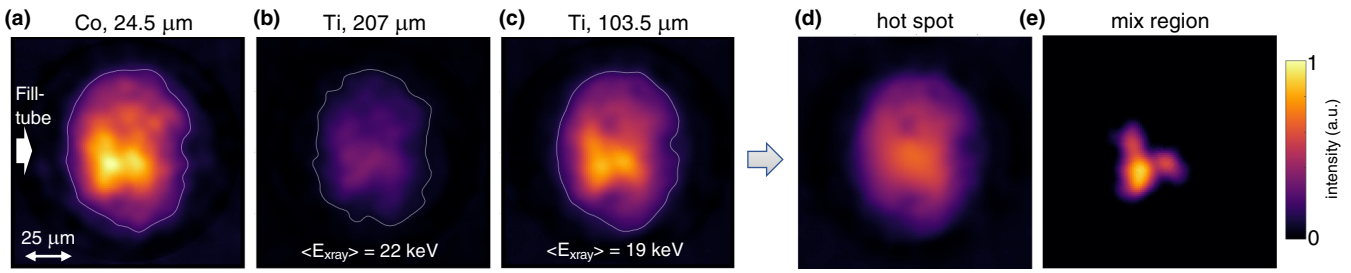

FIG. 2. (a)–(c) Differentially filtered, reconstructed penumbral images of the hot spot from (90 to 100) line-of-sight. (d) X-ray image of the hot spot without the local mix feature from the 103.5 μm titanium channel. (e) X-ray image of the extracted mix region with normalized color scale. Images in (a)–(d) are on the same color scale.

penumbral image [19], in which we separate the image into high and low spatial frequency components. The high-frequency component is then used to locate the bright region. Moreover, a mask over this bright region is created via 2D-biharmonic spline interpolation [28] to produce a hot-spot image without the bright region [see Fig. 2(d)].

The image of the localized bright x-ray distribution is obtained by subtracting the pseudo-homogenous hot-spot image from the original image. Results are shown in Fig. 2(e). As the mask is designed to slightly overfill the localized bright region, this subtraction method results in a robust determination of the bright region. Effectively, its significantly larger surrounding emission subtracts to zero.

After separating the bright region with mix from the surrounding hot spot using the same mask region in each channel, and using the intrinsic coregistration properties of penumbral images to spatially align the channels, we use a Monte Carlo forward-fitting technique [29] to calculate the electron temperatures of both the bright mix region and the surrounding hot spot. This is achieved by matching ratios of integrated, synthetic bremsstrahlung emission spectra to measured ratios of detected x-ray emission coefficients by χ^2 minimization [30]. Here, we use the same temperature (T_e) dependency of the high-energy tail on the bremsstrahlung radiance ϵ as a function of x-ray energy ($h\nu$) as in Ref. [29],

$$\epsilon(h\nu) \propto \frac{\exp(h\nu/T_e)}{(h\nu)^{\alpha}}, \tag{1}$$

with $\alpha = 0.39$ for D-T, $\alpha = 0.31$ for beryllium, and $\alpha = -0.19$ for copper. These values for α are determined by fitting the high-energy tail of spectral radiances from detailed configuration accounting tables [31,32]. Note the value of α has a small effect on the derivative of the x-ray emission spectra.

Error propagation is performed through Monte Carlo sampling of the uncertainties in measured signal ratios, plasma composition, image plate detector sensitivity, and absorption in the materials traversed by the x-rays by applying nontrivial error probability functions [33]. The error bars quoted for electron temperatures reported here are ± 1 standard deviation of the approximately normal distributed electron temperature histograms [compare Fig. 3(b)]. These histograms represent the statistical temperature probability distributions due to those uncertain quantities only and do not contain possible systematic errors. We note that, among others, one possible source of such error is a systematic over- or underprediction of the brightness in the previously described interpolated hot-spot region. Based on self-consistency tests with synthetic data, we can assume that such systematic over- or underprediction is approximately compensated when taking the ratio of the x-ray channels as described above. In addition, we calculated the temperatures with two statistically independent subsets of penumbral images from each x-ray energy channel, which yielded, within statistical error bars, the same results.

Expanding the formalism of Ref. [29], we use the two titanium channels and additionally a cobalt channel [24.5 ± 0.5 μm thickness; see Fig. 2(a)], which is more sensitive to the Be-shell absorption. This combination allows to simultaneously solve for temperature and shell optical depth $\tau = \kappa\,\rho R$, where κ is the shell opacity and ρR is the shell areal density.

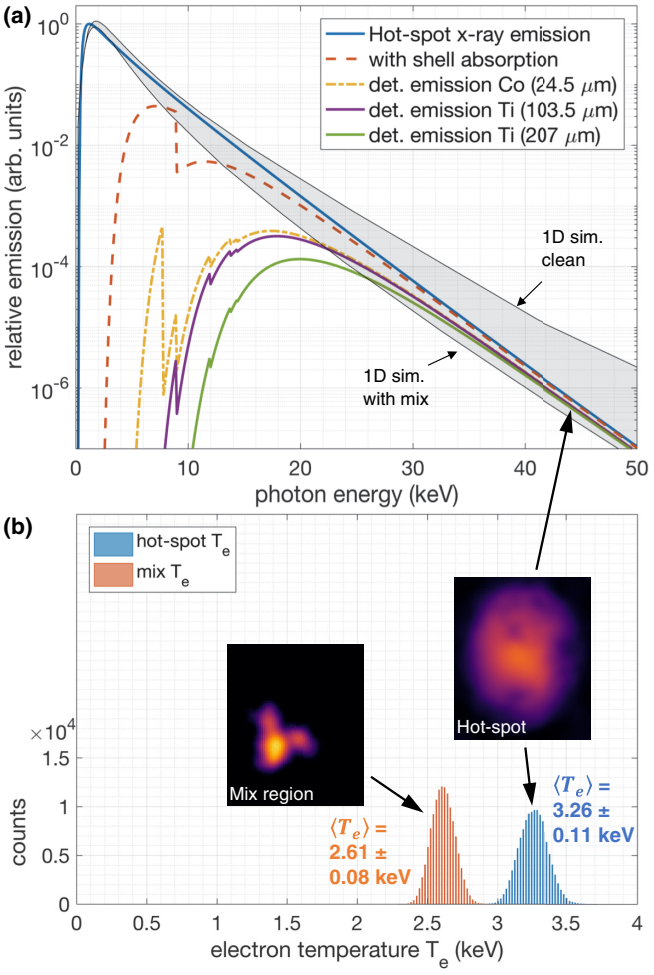

FIG. 3. (a) Calculated x-ray emission spectra for the self-emission of the pseudohomogeneous hot spot including shell absorption and additional filtration. The gray shaded area is bound by predictions from a clean 1D simulation and one that includes a mix model to match the observed nuclear yield and down-scattered neutron ratio. (b) Histograms representing the electron temperature probability distributions in the mix region and in the hot D-T plasma inferred by Monte Carlo sampling of the experimental data using uncertainties of plasma composition, shell optical depth, filter thicknesses, detected photon yield, and image plate detector response.

For that goal, we used the mass attenuation coefficient of cold beryllium and copper from NIST [34] and randomly vary the remaining copper fraction between zero and 2.7%. The upper bound represents the peak dopant fraction of the shell. The temperature of the pseudohomogeneous hot spot [see Fig. 2(d)] is found to be 3.3 ± 0.2 keV together with a shell optical depth at 18 keV of $\tau = 0.46 \pm 0.11$. We find very similar results if we apply the previously published technique [29] with the inferred shell optical depth and using the two titanium filters only, resulting in a temperature of 3.26 ± 0.11 keV.

IV. RESULTS AND DISCUSSION

Figure 3(a) shows the most probable, normalized hot-spot emission spectrum that results from the analysis

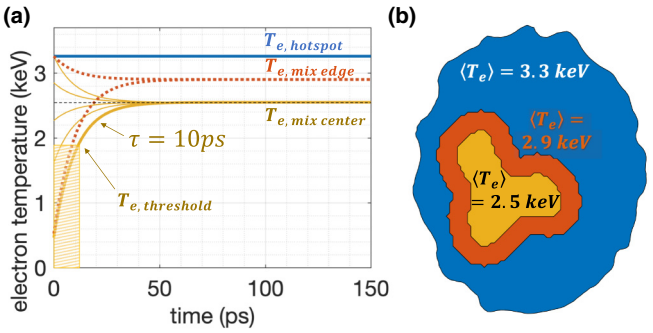

FIG. 4. (a) Simplified picture of the temperature evolution in the mix with different possible initial conditions for the mix center (solid yellow) and mix edge (dotted red) assuming a temperature equilibration time of $\tau = 10$ ps and a constant D-T temperature (solid blue). Early times (shaded) may not be present in the measured, time-integrated x-ray images as the x-ray emission is below the detection threshold at those temperatures. (b) Sketch of the regions that have been spatially resolved and the inferred temperatures.

described above. It also displays spectra from a 1D radiation-hydrodynamics simulation without mix and one that includes a mix model to match the observed nuclear yield and down-scattered neutron ratio only [25]. For better comparison, these data have been normalized matching their mean peak emission and show good agreement with the experimentally inferred hot-spot spectrum. For reference, the lowest ion temperature from D-D reactions, measured by the neutron time-of-flight detectors, which sets an upper limit for the plasma temperature [29,35,36], is 3.27 ± 0.28 keV, consistent with our inferred electron temperature in the pseudohomogeneous hot-spot image.

We now apply the same Monte Carlo technique to the localized bright region [Fig. 2(e)]. Here the presence of higher-Z elements, which radiate more efficiently, represent a significant energy sink in the energy balance of the mix region. Since we do not know the fractions of D-T, Be, and Cu in this region, we use Monte Carlo sampling that combines DCA spectra of the three possible plasma constituents and randomly varies their fractions. We find a mix temperature of 2.61 ± 0.08 keV, which is insensitive to the plasma composition. The corresponding temperature probability distribution is shown in Fig. 3(b). The significant reduction of the temperature in the mix (660 ± 130 eV lower mix temperature than the surrounding hot-spot plasma) demonstrates that the observed strongly enhanced x-ray emission occurs at a locally reduced electron temperature.

The temperature gradients occurring in the hot spot can be further investigated by dividing the mix region into an envelope and the central region [cf. Fig. 4(b)]. We define the envelope's width by our current spatial resolution, 5 μm. For both subparts, the analysis can be done as described above. With this additional subdivision, we obtain a temperature of the mix envelope of 2.9 ± 0.16 keV, that is, between the average mix and D-T temperatures. The central chords of the mix are, however, even cooler than the total average of the mix region: 2.55 ± 0.09 keV. A sketch of these different regions and their temperatures is shown in Fig. 4(b).

We can estimate the absolute energy that is lost from the mix region via continuum radiation from the x-ray flux detected and calculate losses in the hot D-T plasma. The latter is given in unit of GJ by [37]

$$Q_{DT} = 3.1 \times 10^7\ \rho_{DT}\ m_{DT}\ \sqrt{T}\ \delta_{\mathrm{nuc}}. \tag{2}$$

As most neutrons are generated in the hotter D-T plasma, we can employ the flux of fusion neutrons to infer a hot-spot density of $\rho_{DT} = 53 \pm 12$ g/cm^3, with a mass of $m_{DT} = (2.4 \pm 0.5) \times 10^{-6}$ g [25]. The nuclear burn-width of $\delta = 148 \pm 30$ ps corresponds to the burn-width of the x-ray emission. These inputs yield a radiative loss from hot D-T of 1.0 ± 0.4 kJ.

The energy loss ratio between the mixed and unmixed regions of the hot spot is calculated by forward fitting and Monte Carlo sampling including all uncertainties of input parameters. We note that the integrated x-ray energy loss from the mix region strongly depends on the fraction of copper, which introduces additional free-bound emission above 9 keV. This procedure yields low radiation losses of 28 ± 6 J for the extreme case that the mix contains only material from the initially doped layer, and 310 ± 76 J assuming pure beryllium in the mix region. The inferred losses increase further up to 380 ± 89 J if beryllium is diluted with 99% D-T. Future radiation loss measurements may strongly reduce the uncertainty by using materials without significant bound-free emission features. Such future experiments could therefore provide a strong constraint for validating new mix models that aim to describe localized mix. Furthermore, a local temperature deficit also impacts the determination of radiation losses as lower temperatures result in a steeper spectral gradient at high x-ray energies. For example, the energy loss from the mix region is 3.2 times higher here than it would be inferred if the mix was assumed to be in thermal equilibrium with the hot D-T plasma.

The observed temperature difference between regions with and without mix drives an energy flow into the cooler part. In general, it is important to know if our time-integrated signal is the average of a dynamically evolving system or represents a quasi-equilibrium mix temperature. Originating from the ablator, the mix will initially be much colder than the D-T plasma and radiative losses will be small. Without radiation losses, the mix temperature obeys

$$\frac{dT_{\mathrm{mix}}}{dt} = \frac{T_{DT} - T_{\mathrm{mix}}}{\tau}, \tag{3}$$

where the time constant τ is determined by the total heat flow into the region and its heat capacity ($c_{\mathrm{mix}} \sim 10^{-7}$ J/K). The heat flow via conduction is given by

$$Q_{\mathrm{cond}} = c_{\mathrm{mix}} \frac{dT_{\mathrm{mix}}}{dt} = \int dA\ \kappa_{\mathrm{cond}}\ \nabla T. \tag{4}$$

Here the integral is to be taken over the surface area of the mixed region. κ_{cond} is the electron heat conduction, which we estimate to be on the order of 10^8 Jm^{-1}K^{-1}s^{-1} [38]. The temperature gradient can be estimated by the temperature difference over its length scale; its lower bound is the electron mean-free path (0.5 μm), and its upper bound the radius of the mix region, i.e., approximately 7 μm. With these input data, we obtain a rapid rise of the mix temperature on a timescale

of a few, up to tens of picoseconds. This is shown in Fig. 4(a), which displays a simplified, quasistatic picture of the mix temperature evolution with constant hot-spot temperature. While the hot-spot temperature will rise to a peak during compression and subsequently fall during decompression, this figure illustrates that a locally reduced electron temperature can be quickly established and maintained during the implosion.

The bold, solid yellow line may represent a worst case, where cold material is injected right at the beginning of the burn. If it is injected earlier as suggested by time-resolved imaging, it will track the hot-spot temperature more closely as the plasma is compressed. Thus, we conclude that, while at a locally reduced temperature, the mix region is in a quasistationary state where energy gain by conduction and radiative losses balance for most of the emission time.

Since we have a balance between heat input through conduction and radiation losses, we can also estimate the total radiation losses from the stationary condition $Q_{\mathrm{cond}} - Q_{\mathrm{rad}} = 0$, close to peak compression. Of course, the temperature in the mix is here the key quantity as both heat source and sink strongly depend on it. With our estimates for the heat transfer from the hot D-T plasma to the mix, and assuming a spherical mix surface area, we obtain low radiation losses of 12 J if we assume the radius of the mix region (7 μm) as the temperature gradient length scale, and 170 J if we assume the length scale to be equal to the electron mean-free path. These energies increase linearly when the surface area is increased at constant volume and are consistent with the losses inferred from the x-ray spectrum. More precise calculations would require additional information on the 3D shape of the mix region and its temperature distribution.

V. CONCLUSIONS

In summary, we have developed a technique to determine spatial temperature variations in the central plasma of a spherically imploding shell. Using penumbral imaging with large apertures allows for large throughputs and probing with hard x-rays that are less susceptible to absorption by the surrounding material and increases spatial resolution. The present resolution of 5 μm allows to resolve strongly radiating features in NIF implosions. For such a zone, we find a significant temperature deficit compared to the hot D-T plasma around it indicating large localized energy losses. Contrary to intuition, cooler regions radiate more strongly in our case; indeed, they are cooler because they radiate strongly. The estimated heat flow into the mix region is consistent with the spectrally inferred radiation losses. Moreover, we find that the mix quickly establishes an equilibrium where heat conduction into the mix region and radiative losses balance. Thus, localized mix results in a continuous energy loss during the confinement of the hot spot. Our measurement of local temperatures yields important information for mix mitigation strategies, e.g., a reduced fill-tube diameter [39,40]. Besides ICF, this technique can also contribute to quantify mix features in science experiments that create and study extreme conditions by spherical implosions [41–43].

ACKNOWLEDGMENTS

This work was performed under the auspices of the U.S. Department of Energy by Lawrence Livermore National Laboratory under Contract DE-AC52-07NA27344. D.O.G. thanks the Lawrence Livermore National Laboratory for its support and hospitality.

[1] R. Betti and O. A. Hurricane, Inertial-confinement fusion with lasers, Nature Phys. **12**, 435 (2016).

[2] M. J. Edwards *et al.*, The experimental plan for cryogenic layered target implosions on the National Ignition Facility—The inertial confinement approach to fusion, Phys. Plasmas **18**, 051003 (2011).

[3] J. D. Lindl *et al.*, The physics basis for ignition using indirect-drive targets on the National Ignition Facility, Phys. Plasmas **11**, 339 (2004).

[4] E. I. Moses *et al.*, The National Ignition Facility: Ushering in a new age for high energy density science, Phys. Plasmas **16**, 041006 (2009).

[5] J. D. Lindl, Development of the indirect-drive approach to inertial confinement fusion, and the target physics basis for ignition, and gain, Phys. Plasmas **2**, 3933 (1995).

[6] B. A. Hammel *et al.*, High-mode Rayleigh-Taylor growth in NIF ignition capsules, High Energy Density Phys. **6**, 171 (2010).

[7] C. R. Weber *et al.*, Three-dimensional hydrodynamics of the deceleration stage in inertial confinement fusion, Phys. Plasmas **22**, 032702 (2015).

[8] V. A. Smalyuk *et al.*, Mix and hydrodynamic instabilities on NIF, JINST **12**, C06001 (2017).

[9] B. M. Haines *et al.*, The effects of convergence ratio on the implosion behavior of DT layered inertial confinement fusion capsules, Phys. Plasmas **24**, 072709 (2017).

[10] D. S. Clark *et al.*, Capsule physics comparison of National Ignition Facility implosion designs using plastic, high density carbon, and beryllium ablators, Phys. Plasmas **25**, 032703 (2018).

[11] O. A. Hurricane *et al.*, Fuel gain exceeding unity in an inertially confined fusion implosion, Nature (London) **506**, 343 (2014).
[12] L. Divol *et al.*, Symmetry control of an indirectly driven high-density-carbon implosion at high convergence and high velocity, Phys. Plasmas **24**, 056309 (2017).
[13] S. Le Pape *et al.*, Fusion Energy Output Greater than the Kinetic Energy of an Imploding Shell at the National Ignition Facility, Phys. Rev. Lett. **120**, 245003 (2018).
[14] S. P. Regan *et al.*, Hot-spot mix in ignition-scale implosions on the NIF, Phys. Plasmas **19**, 056307 (2012).
[15] S. P. Regan *et al.*, Hot-Spot Mix in Ignition-Scale Inertial Confinement Fusion Targets, Phys. Rev. Lett. **111**, 045001 (2013).
[16] T. Ma *et al.*, Onset of Hydrodynamic Mix in High-Velocity, Highly Compressed Inertial Confinement Fusion Implosions, Phys. Rev. Lett. **111**, 085004 (2013).
[17] T. Ma *et al.*, The role of hot spot mix in the low-foot and high-foot implosions on the NIF, Phys. Plasmas **24**, 056311 (2017).
[18] B. A. Hammel *et al.*, Diagnosing and controlling mix in National Ignition Facility implosion experiments, Phys. Plasmas **18**, 056310 (2011).
[19] M. A. Barrios *et al.*, Experimental investigation of bright spots in broadband, gated x-ray images of ignition-scale implosions on the National Ignition Facility, Phys. Plasmas **20**, 072706 (2013).
[20] L. A. Pickworth *et al.*, Visualizing deceleration-phase instabilities in inertial confinement fusion implosions using an "enhanced self-emission" technique at the National Ignition Facility, Phys. Plasmas **25**, 054502 (2018).
[21] A. B. Zylstra *et al.*, Beryllium capsule implosions at a case-to-capsule ratio of 3.7 on the National Ignition Facility, Phys. Plasmas **25**, 102704 (2018).
[22] J. L. Kline *et al.*, First beryllium capsule implosions on the National Ignition Facility, Phys. Plasmas **23**, 056310 (2016).
[23] A. N. Simakov *et al.*, Performance of beryllium targets with full-scale capsules in low-fill 6.72-mm hohlraums on the National Ignition Facility, Phys. Plasmas **24**, 052704 (2017).
[24] E. N. Loomis *et al.*, Implosion shape control of high-velocity, large case-to-capsule ratio beryllium ablators at the National Ignition Facility, Phys. Plasmas **25**, 072708 (2018).
[25] A. B. Zylstra *et al.*, Implosion performance of subscale beryllium capsules on the NIF, Phys. Plasmas **26**, 052707 (2019).
[26] B. Bachmann *et al.*, X-ray penumbral imaging diagnostic developments at the National Ignition Facility, Proc. SPIE **10390**, 103900B (2017).
[27] B. Bachmann *et al.*, Resolving hot-spot microstructure using x-ray penumbral imaging (invited), Rev. Sci. Instrum. **87**, 11E201 (2016).
[28] D. T. Sandwell, Biharmonic spline interpolation of GEOS-3 and SEASAT altimeter data, Geophys. Res. Lett. **14**, 139 (1987).
[29] L. C. Jarrott *et al.*, Thermal Temperature Measurements of Intertial Fusion Implosions, Phys. Rev. Lett. **121**, 085001 (2018).
[30] B. Bachmann *et al.*, High-speed three-dimensional plasma temperature determination of axially symmetric free-burning arcs, J. Phys. D **46**, 125203 (2013).
[31] S. J. Rose, Calculations of the radiative opacity of laser-produced plasmas, J. Phys. B **25**, 1667 (1992).
[32] H. A. Scott and S. B. Hansen, Advances in NLTE modeling for integrated simulations, High Energy Density Phys. **6**, 39 (2010).
[33] L. C. Jarrott *et al.*, Hot-spot electron temperature from x-ray continuum measurements on the NIF, Rev. Sci. Instrum. **87**, 11E534 (2016).
[34] J. H. Hubbell and S. M. Seltzer, Tables of X-ray mass attenuation coefficients and mass energy-absorption coefficients 1 keV to 20 MeV for elements Z = 1 to 92 and 48 additional substances of dosimetric interest, National Institute of Standards and Technology, Internal Report NISTIR 5632, 1995.
[35] D. H. Munro *et al.*, Impact of temperature-velocity distribution on fusion neutron peak shape, Phys. Plasmas **24**, 056301 (2017).
[36] T. J. Murphy, The effect of turbulent kinetic energy on inferred ion temperature from neutron spectra, Phys. Plasmas **21**, 072701 (2014).
[37] O. Hurricane *et al.*, Approaching a burning plasma on the NIF, Phys. Plasmas **26**, 052704 (2019).
[38] P. Sterne (private communication, 2019).
[39] A. G. MacPhee *et al.*, Hydrodynamic instabilities seeded by the x-ray shadow of ICF capsule fill-tubes, Phys. Plasmas **25**, 082702 (2018).
[40] A. Pak *et al.*, The impact of localized radiative loss on inertial confinement fusion implosions (unpublished).
[41] D. T. Casey *et al.*, Thermonuclear reactions probed at stellar-core conditions with laser-based inertial-confinement fusion, Nature Phys. **13**, 1227 (2017).
[42] W. Theobald *et al.*, Time-resolved compression of a capsule with a cone to high density for fast-ignition laser fusion, Nat. Commun. **5**, 5785 (2014).
[43] D. B. Sayre *et al.*, Neutron Time-of-Flight Measurements of Charged-Particle Energy Loss in Inertial Confinement Fusion Plasmas, Phys. Rev. Lett. **123**, 165001 (2019).